Is J enough? Comparison of gravitational waves emitted along the total angular momentum direction with other preferred orientations

R. O'Shaughnessy

Center for Gravitation and Cosmology, University of Wisconsin-Milwaukee, Milwaukee, WI 53211, USA*

J. Healy, L. London, Z. Meeks, and D. Shoemaker

Center for Relativistic Astrophysics, Georgia Tech, Atlanta, GA 30332, USA

The gravitational wave signature emitted from a merging binary depends on the orientation of an observer relative to the binary. Previous studies suggest that emission along the total initial or total final angular momenta leads to both the strongest and simplest signal from a precessing compact binary. In this paper we describe a concrete counterexample: a binary with $m_1/m_2 = 4$, $a_1 = 0.6\hat{x} = -a_2$, placed in orbit in the x, y plane. We extract the gravitational wave emission along several proposed emission directions, including the initial (Newtonian) orbital angular momentum; the final ($\simeq$ initial) total angular momentum; and the dominant principal axis of $\langle L_{(a}L_{b)}\rangle_M$. Using several diagnostics, we show that the suggested preferred directions are not representative. For example, only for a handful of other directions ($p \lesssim 15\%$) will the gravitational wave signal have comparable shape to the one extracted along each of these fiducial directions, as measured by a generalized overlap (> 0.95). We conclude that the information available in just one direction (or mode) does not adequately encode the complexity of orientation-dependent emission for even short signals from merging black hole binaries. Future investigations of precessing, unequal-mass binaries should carefully explore and model their orientation-dependent emission.

I. INTRODUCTION

Numerical simulations of merging compact binaries produce a gravitational wave signature that depends on the orientation of the binary relative to the line of sight. For nonprecessing comparable-mass binaries, this orientation dependence can be well-modeled as purely quadrupolar emission from conjugate and orthogonal $l = |m| = 2$ modes. In this approximation, only one complex-valued function is needed to characterize the gravitational wave signature from a binary: either the $(l, m) = (2, 2)$ mode itself or the strain extracted along the binary angular momentum axis. This approach has been broadly adopted when comparing nonspinning numerical relativity simulations to one another [1] and to post-Newtonian [2–5] and other [6] approximations; when building hybrid waveforms that join systematic post-Newtonian approximations to numerical relativity [7, 8]; when constructing phenomenological approximations to numerical relativity waveforms [9–11]; and when searching for the gravitational wave signature of merging compact binaries with interferometric detectors [12]. For similar reasons, the gravitational wave signature from a nonprecessing unequal-mass binary can also be approximated by $h_{+,\times}(t, \hat{J})$, the radiation along the total angular momentum axis $\hat{J}$.

Motivated by this approximation, some have proposed that radiation along "the total angular momentum direction" is a fiducial example of the gravitational wave signature from a binary [13]. In general, the total angular momentum direction $\hat{J}$ is not conserved during the inspiral [14] and coalescence [15–17]. To a good approximation, however, the orbital angular momentum often precesses around the total angular momentum [14]. During the inspiral, the binary radiates predominantly along the instantaneous orbital angular momentum [14, 18–20], which precesses around the total angular momentum. In this case, previous direct and indirect calculations suggest that that strong, simple emission will occur along the *average* direction, which for simple precession corresponds to the total angular momentum [13, 21]. In this paper, we provide an explicit counterexample, for which $\hat{J}$ neither corresponds to nor produces radiation similar to the peak emission direction. We contrast $\hat{J}$ with the time-dependent and signal-averaged directions from $\langle L_{(a}L_{b)}\rangle$ [21], which better reflects the peak emission direction. Finally, we explicitly demonstrate that higher harmonics and precession prevent a significant fraction of orientations from being well-fit as the linear superposition of only two basis waveforms in an "antipodal decomposition." The orientation-dependent emission of precessing waveforms is unavoidably more complicated than the response of their nonprecessing counterparts.

A. Context

Merging binaries imprint their properties on the gravitational waves radiated to infinity in all directions [1]. In practice, however, gravitational wave detectors have access to only one line of sight, sometimes only one polarization. Under the right circumstances, two physically distinct configurations can produce very similar emission in the detectors' sensitive band. These near-degeneracies complicate source parameter estimation [22–27] and thus

the interpretation of gravitational wave measurements for astrophysics.

Conversely, a single source can produce highly dissimilar signals along different lines of sight. By contrast, the signal template used in real searches for nonprecessing binaries in gravitational wave data assumes a universal form for all orientations: a linear superposition of two basis functions, the "cosine" and "sine" chirps [12]. For nonprecessing binaries, this signal model is physically well-motivated [see the Appendix]; the relative weights of the modes are in one-to-one relation to the source inclination relative to the line of sight. In this paper we use a concrete example where this decomposition fails. For the example described in this paper, more than two functional degrees of freedom are needed to reproduce the gravitational wave signal accurately for all lines of sight.

II. ORIENTATION-DEPENDENT EMISSION

We simulated the evolution of a binary black hole (BBH), with total mass $M = m_1 + m_2 = 1.0$ and mass ratio $m_1/m_2 = 4$, initiated on the x-axis, with initial separation $d = 9$ and initial dimensionless spin vectors $\mathbf{a}_1 = 0.6\hat{x} = -\mathbf{a}_2$. For reference, the initial and final total angular momenta are

$$J_i = 0.36\hat{x} + 0.60\hat{z} \tag{1}$$

$$J_f = 0.27\hat{x} + 0.036\hat{y} + 0.49\hat{z} \tag{2}$$

Initial data was evolved with Maya, which was used in previous BBH studies [28–36]. The grid structure for each run consisted of 10 levels of refinement provided by CARPET [37], a mesh refinement package for CACTUS [38]. Sixth-order spatial finite differencing was used with the BSSN equations implemented with Kranc [39]. The outer boundaries are located at 307M. Each simulation was performed with a resolution of $M/140$ on the finest refinement level, with each successive level's resolution decreased by a factor of 2. In the text, we present results for the fiducial $r = 90$ extraction radius and for this resolution. The comparatively large differences we describe exist at all large extraction radii and simulation resolutions we have explored. Similarly, though we adopt fiducial snapshot parameters (time and mass) to generate the contours in Figures 1 and 2, we find similar behavior at neighboring masses and times.

This simulation has markedly anisotropic emission. Figure 1 shows contours of $|\psi_4|$ (solid) and $dE/dtd\Omega \propto |\int \psi_4 dt|^2$ (dashed), superimposed with black dots indicating the total angular momentum direction and a blue dot indicating the dominant eigenvector of $\langle L_{(a}L_{b)}\rangle$ [21]. This tensor is defined by

$$\langle L_{(a}L_{b)}\rangle_M = \frac{\int_{-\infty}^{\infty} df \int d\Omega \tilde{\psi}_4^*(f) L_{(a}L_{b)} \tilde{\psi}_4(f)/S_h}{\int_{-\infty}^{\infty} df \int d\Omega |\tilde{\psi}_4(f)|^2/S_h} \tag{3}$$

where S_h is the noise power spectrum of a candidate interferometer. None of these three directions corresponds to the directions of peak transverse tidal force or radiated power.

For clarity we only show contours for a single time. Over the inspiral, the beampattern evolves slightly, with the orientation of strongest ψ_4 and dE/dt roughly following the path of our preferred orientation (blue line). For all times simulated, the largest ψ_4 and $dE/dtd\Omega$ is never along the total angular momentum.

For comparison, in the bottom panel of Figure 1 we show contours for a simulation with comparable mass ratio in the absence of spin. Though vertically symmetric, the functional form of ψ_4 and $dE/dtd\Omega$ is largest at specific angle ϕ that evolves along with the (retarded) separation vector. For this particular timeslice, the peak occurs at $(\theta, \phi) \simeq (0.5, 1.5)$, significantly offset from the angular momentum axis. This shape rotates at the orbital period through merger. By contrast, all three preferred orientations (L, J and $\hat{V}$, the principal eigendirection of $\langle L_{(a}L_{b)}\rangle$) always lie along the $\hat{z}$ axis.

For data analysis purposes, a more relevant orientation-dependent quantity is the coherent signal-to-noise accessible to a particular detector network along that line of sight. Under the simplifying assumptions that two identical interferometers misaligned by $\pi/4$ intercept gravitational wave emission perpendicular to the line of sight, an idealized orientation-dependent signal-to-noise ratio $\rho(\hat{n})$ is given by [21, 40][1]

$$\rho^2 \equiv 2 \int_{-\infty}^{\infty} \frac{df}{S_h} \frac{|\psi_4(f, \hat{n})|^2}{(2\pi f)^4} \tag{4}$$

where S_h is the noise power spectrum of each of the two interferometers. (This expression is simply the sum of the signal to noise due to each detector $(\rho_1^2 + \rho_2^2)$, using $\psi_4 = \partial_t^2(h_+ - ih_\times)$ to relate the sum to a quantity naturally produced by simulations.) The dotted contours in Figure 2 show contours of constant ρ, adopting a simple analytic model for the initial LIGO noise curve [41] and a fiducial total mass $M = 100M_\odot$ for the binary to scale our (dimenionless) simulations. Again, neither the total nor (Newtonian) orbital angular momentum direction seems significant with respect to the detectable signal power.

The contours of ρ^2 and its peak location inevitably are qualitatively similar to contours of $dE/dfd\Omega$, the energy radiated per unit frequency. The expression for $\rho^2(M)$ can be rewritten as a suitable frequency-weighted average of $dE/dfd\Omega \propto |\tilde{\psi}_4/f|^2$. For a suitable choice of f, contours in the neighborhood of the maximum are qualitatively similar.

---

[1] For comparison, the orientation-averaged signal to noise $\bar{\rho}$ described in O'Shaughnessy et al. [40] is precisely the orientation average $\langle \rho^2 \rangle$ of our signal-to-noise ratio over all emission directions.

Two- or more detector networks are generally sensitive to gravitational wave polarization. Our cartoon two-detector network has equal sensitivity to both polarizations. Such a network can automatically project out left- or right-handed signal. Motivated by sensitivity to helicity, we define two signal to noise ratios $\rho_\pm$ that measure sensitivity to right and left handed emission, respectively:

$$\rho_+^2 \equiv 2 \int_0^\infty \frac{df}{S_h} \frac{|\psi_4(f,\hat{n})|^2}{(2\pi f)^4} \tag{5}$$

$$\rho_-^2 \equiv 2 \int_{-\infty}^0 \frac{df}{S_h} \frac{|\psi_4(f,\hat{n})|^2}{(2\pi f)^4} \tag{6}$$

At each instant, right-handed emission occurs along the orbital angular momentum direction, left-handed opposite. These expressions encode the contributions of right-handed and left-handed emission to the total SNR $\rho^2 = \rho_-^2 + \rho_+^2$. The solid curves in Figure 2 are contours of ρ_+. Their shape and similarity to contours of ρ demonstrate that each of the two local extrema of ρ^2 is produced near-exclusively by emission with a single handedness. Neither local extrema corresponds to the direction of J or the (Newtonian) orbital angular momentum. By contrast, the nearly-antipodal extrema do correspond to the orientation of the principal eigenvalue of $\langle L_{(a}L_{b)} \rangle_M$ [21], shown as a red dot in Figure 2.

To summarize, for our fiducial binary, we have examined the gravitational wave signature along three common choices for the preferred orientation: the principal axis of $\langle L_{(a}L_{b)} \rangle_M$ as well as the (Newtonian) orbital and total angular momentum directions. Neither angular momentum direction corresponds to a direction extremizing strain, energy flux, or detectable signal to noise. By contrast, the direction identified by $\langle L_{(a}L_{b)} \rangle_M$ nearly corresponds to a local maximum of the signal-to-noise ρ^2. We anticipate and will show below that the direction identified by $\langle L_{(a}L_{b)} \rangle_M$ is "more representative" of the orientation-dependent emission, in that a greater fraction of the orientation-dependent emission can be well-fit by it. However, none of the three directions can adequately fit all the complexities of this binary's orientation-dependent emission, even for one representative mass $M = 100 M_\odot$.

III. CONTRASTING DIFFERENT ORIENTATIONS

Most variations in the gravitational wave signature or amplitude along different emission directions are too subtle to be distinguished by gravitational wave networks at the amplitude of astrophysically plausible signals. Generally, distinguishability of signals depends strongly on the detector network, signal model, and source location relative to the earth. Rather than address this complicated issue in general, we adopt a simple physically-motivated proof of concept calculation. The complications associated with real detector networks will, if anything, further
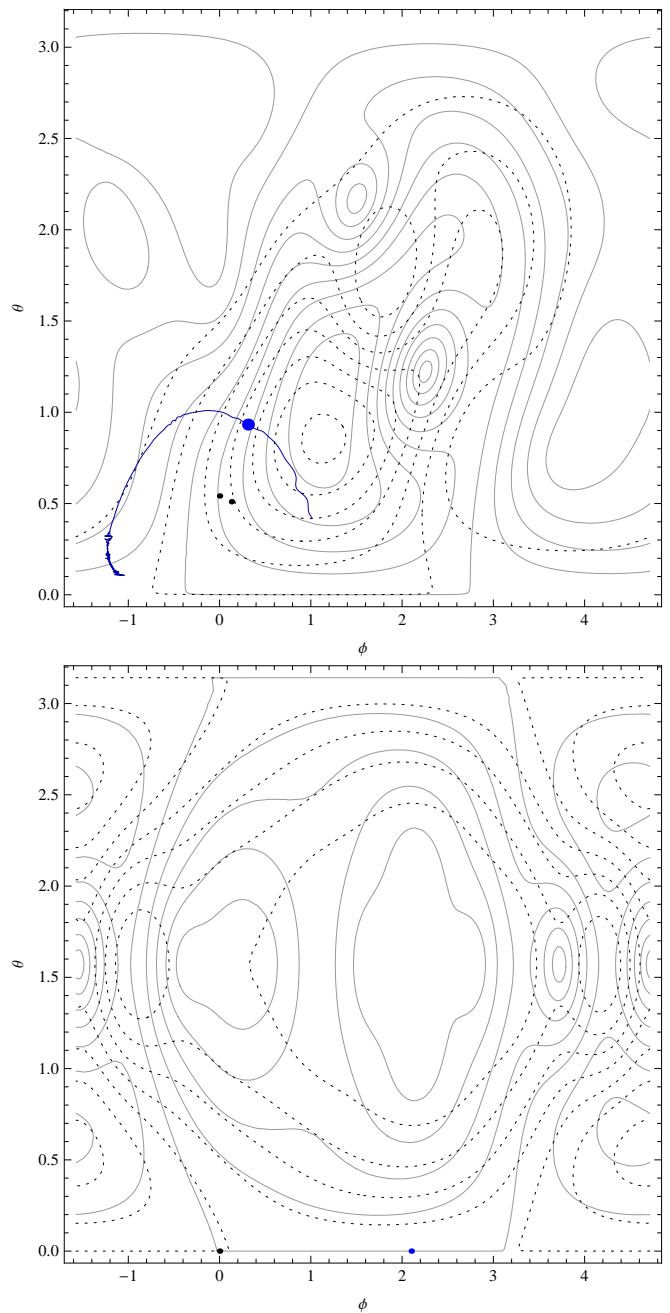

FIG. 1: **Time-domain contours** of $|\psi_4|$ (solid) and $dE/dtd\Omega$ (dashed), evaluated at the peak of the $(l,m) = (2,2)$ mode. Both quantities are normalized to 1 at $\theta = \phi = 0$. Solid black dots indicate the location of the initial and final total angular momenta. The solid blue dot indicates the preferred axis identified by $\langle L_{(a}L_{b)} \rangle_t$ at this time. The dark blue path indicates how this preferred orientation evolves with time, several hundred M before and $30M$ after this reference time. The *top panel* corresponds to the fiducial spinning binary. The bottom panel shows a binary with comparable mass ratio $(m_1/m_2 = 4)$ but without any spin.
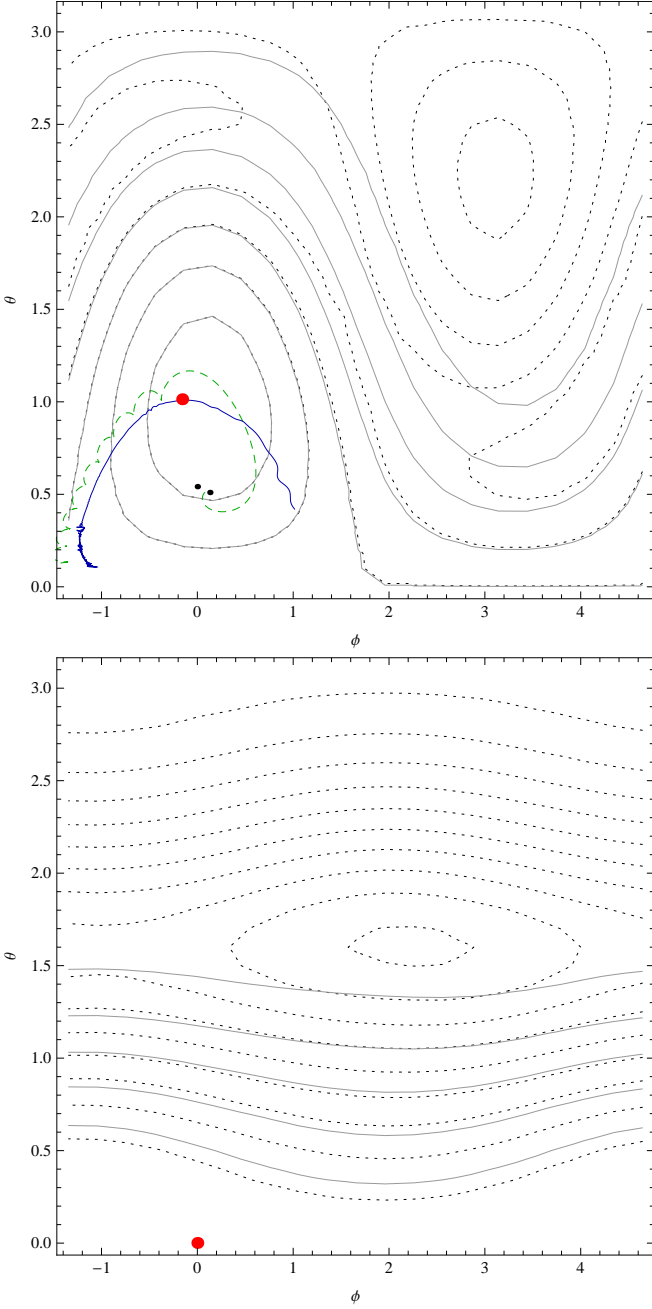
FIG. 2: **Detector-weighted contours** of ρ (dotted) and ρ_+ (solid), evaluated at $M = 100 M_\odot$, plotted versus the simulation's asymptotic spherical polar coordinates (i.e., aligned with the initial orbital angular momentum). Solid black dots indicate the location of the initial and final total angular momenta. The solid red dot indicates the preferred axis identified by $\langle L_{(a} L_{b)} \rangle_{M,+}$ [Eq. (A1)] at this time; nearly identical preferred axes are identifies by $\langle L_{(a} L_{b)} \rangle_M$ and $\langle L_{(a} L_{b)} \rangle_{M-}$. As in Fig. 1, the solid blue path indicates the evolution of $\langle L_{(a} L_{b)} \rangle$ versus time. The dashed green path indicates the orientation of the (Newtonian, coordinate) orbital angular momentum $\propto \mathbf{r} \times \mathbf{v}$. The *top panel* corresponds to the fiducial spinning binary, while the *bottom panel* shows an nonspinning binary with comparable mass ratio ($q = 4$). In the bottom panel, the preferred orientation identified by $\langle L_{(a} L_{b)} \rangle_{M,+}$ is slightly above the $\theta = 0$ line; the two directions identified by $\langle L_{(a} L_{b)} \rangle_{M,\pm}$ are not precisely antipodal.

break any symmetries connecting the natural emission direction to $\hat{J}$.

First and foremost, we introduce a complex overlap and its natural maximization in time and *polarization*, a tool which efficiently eliminates two extrinsic parameters of generic signals even in the presence of higher harmonics. Though we adopt this complex overlap for technical convenience and its explicit relationship with $\langle L_{(a} L_{b)} \rangle$, all results described below also follow from the standard inner product on a single polarization at a time [Eq. (11); see [42, 43]]. Technically, subtle differences arise due to the number of data streams and the order of maximization over extrinsic parameters: time and polarization (two-detector complex) or time and phase (single-detector match). Practically speaking, however, the two expressions often return comparable results, particularly when one of the two signals is nearly circularly polarized as will be the case below. As an example, in Figure 3 we compare the complex match P to the "typical" and "minimax" matches [42]. In regions of high complex overlap, the two are qualitatively similar. In regions with low complex overlap, the "typical" and "minimax" matches differ substantially, indicating the two linear polarizations along that line of sight are distinguishable and comparable in magnitude.

A. Complex overlap

For each emission direction $\hat{n}$, we once again assume two identical interferometers are placed, oriented by $\pi/4$ relative to one another and perpendicular to the incident signal. We coherently compare the (noise-free) signal expected along any pair of orientations with a complex inner product motivated by the detector's noise power spectrum [21].

For our purposes, numerical relativity simulations take as inputs binary black hole parameters and desired line of sight (denoted by λ) and return the Weyl scalar $\psi_4(t)$, a complex-valued function of time evaluated along that line of sight. For any pair of simulations and lines of sight, we compare ψ_4 and ψ_4' by a complex overlap

$$P(\lambda, \lambda') \equiv \frac{(r\psi_4 | r\psi_4')}{|r\psi_4||r\psi_4|} \tag{7a}$$

$$(A, B) \equiv \int_{-\infty}^{\infty} 2 \frac{df}{(2\pi f)^4 S_h} \tilde{A}(f)^* \tilde{B}(f) \tag{7b}$$

where S_h is a detector strain noise power spectrum. In this and subsequent expressions we used unprimed and primed variables to distinguish between the two waveforms being compared, involving potentially distinct parameters λ' and lines of sight $\hat{n}'$. For simplicity and to avoid ambiguity, in this paper, we adopt a semianalytic model for the initial LIGO sensitivity [41]. As with the single-detector overlap, the complex overlap can be maximized over the event time and *polarization* (t_c, ψ_c) and

by a simple fourier transform:

$$P_{max} \equiv \max_{t_c, \psi_c} |P| \tag{8}$$

$$= \frac{1}{|\psi_4||\psi_4{}'|} \left| \int 2 \frac{df}{(2\pi f)^4 S_h} \tilde{\psi}_4(f)^* \tilde{\psi}_4(f) e^{i(2\pi f t_c + \psi_c)} \right|$$

For a network with isotropic sensitivity to both gravitational wave polarizations,[2] this complex-valued expression naturally characterizes the ability of the network to differentiate signals. The real part of this expression corresponds to a coherent sum of the conventional overlaps of the two gravitational wave polarizations generated from ψ:

$$\mathrm{Re}(\psi_4, \psi_4{}') = \langle h_+ | h'_+ \rangle + \langle h_\times | h'_\times \rangle \tag{9}$$

$$\tilde{h}_+ + i\tilde{h}_\times = -\psi(f)/(2\pi f)^2 \tag{10}$$

$$\langle A | B \rangle = 2 \int_{-\infty}^{\infty} df \, \tilde{A}^* \tilde{B}/S_h \tag{11}$$

where $\langle A | B \rangle$ is the standard single-detector overlap of gravitational wave strain. This expression also relies on the gauge-invariant output of gravitational wave simulations, without any complications associated with conversion $\psi_4 \to h(t)$. Critically, this expression naturally respects rotational symmetry around the line of sight: if the two simulations are rotated by γ, γ', then $\psi_4 \to e^{-2i\gamma}\psi_4$ and similarly, so P changes by a pure phase:

$$P(R\lambda, R'\lambda') = e^{-2i(\gamma' - \gamma)} P(\lambda, \lambda')$$

Equivalently, the absolute value $|P|$ corresponds to choosing the (physically arbitrary) orientations of the two simulations such that P is real. Similarly, the complex overlap interacts transparently with a decomposition of the NR signal into (complex) spin-weighted spherical harmonics. For example, as with the conventional single-detector signal, a network with equal sensitivities to two polarizations has a network Fisher matrix along the line of sight proportional to

$$\Gamma_{ab} = (\partial_a \psi_4, \partial_b \psi_4) \tag{12}$$

For rotations, the Fisher matrix can be reorganized as an action of SU(2) generators on ψ_4 [21]:

$$\Gamma_{ab} = (L_a \psi_4, L_b \psi_4) \tag{13}$$

This action can be evaluated algebraically using the known properties of SU(2).

Qualitatively speaking, the complex overlap is considerably more discriminating than a single-polarization
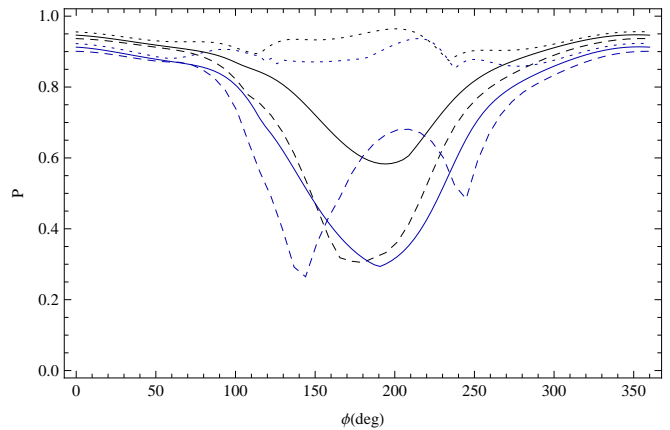

FIG. 3: **Comparison of overlap for complex versus standard match**: These curves compare three different criteria to distinguish between emission along $\hat{z}$ and $\hat{n}(\theta, \phi)$, shown for $\theta = 40.5$ deg (black) and 53 deg (blue). The solid curve is the normalized complex overlap $|P(\hat{z}, \hat{n})|$. The dotted curve and dashed curves are the "typical" and "minimax" match constructed from $h_+, h_\times$ along the two lines of sight [42].

overlap. As an example, because the complex overlap naturally distinguishes between helicities, the complex overlap between the $\hat{z}$ and $-\hat{z}$ directions of an inspiralling nonprecessing binary is nearly 0. By contrast, a single-detector overlap would be nearly unity, as one polarization cannot distinguish between left- and right-handed signals. Finally, in the complex overlap, maximization over the physically irrelevant polarization angle γ corresponds to an absolute value.[3]

B. Area of high overlap

For each of the three reference orientations identified above – $\hat{v} = \hat{z}$, the initial (Newtonian) orbital angular momentum direction; $\hat{J}$, the nearly-conserved final angular momentum direction; and $\hat{V}$, the preferred orientation identified by $\langle L_{(a}L_{b)} \rangle_{M+}$ – we compute $P_{max}(\hat{v}, \hat{n})$ everywhere on the sphere.

For comparison, as indicated by the red curve in Figure 4, for a nonprecessing binary the emission along $+\hat{J} = \hat{z} = \hat{V}$ alone can fit about one third of all emis-

---

[2] Currently-planned gravitational-wave detector networks are primarily sensitive to one polarization for most sky locations [44, 45]. Future gravitational wave networks will try to achieve comparable sensitivity in both polarizations, to better measure source inclination and distance [44].

[3] For a single-detector overlap, maximization over polarization requires diagonalizing a quadratic form for basis waveforms [42]. Physically, this process corresponds to choosing a detector orientation aligned with the natural principal axes of the waveform, projected on the plane of the sky. When multiple harmonics are present, maximization of single-detector overlaps becomes an arduous process; see, e.g., the Appendix of McWilliams et al. [46]. Finally, for the single-detector overlap, efficient maximization over polarization is generally incompatible with fast (fourier-transform-based) determination of the coalescence time [42].
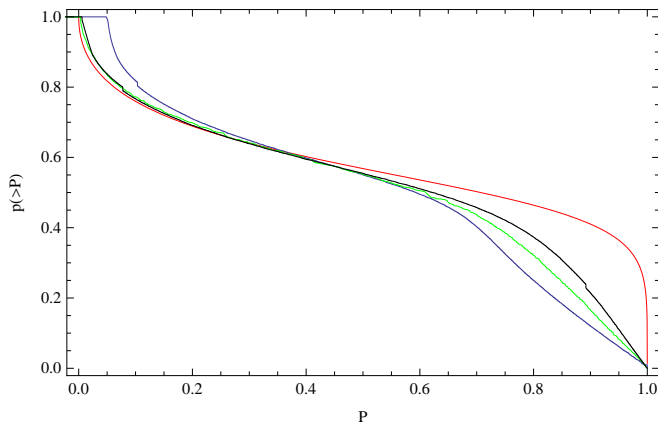
FIG. 4: **Area of high overlap**: Fraction p of the sphere for which the overlap $P_{max}(\hat{v}, \hat{n})$ is above a given threshold P, versus the threshold, for $\hat{v} = \hat{z}$ (blue), $\hat{J}$ (green), and the preferred axis of $\left\langle L_{(a}L_{b)} \right\rangle_M$ (black). For comparison, the thin red curve shows the corresponding result for a binary radiating only conjugate and orthogonal $(2, 2)$ and $(2, -2)$ modes and a reference axis $\hat{v} = \hat{z}$; see the appendix for a derivation. For this idealized nonprecessing binary, more than a third of all orientations have better than $P = 0.95$ (complex) match with the $(2, 2)$ mode; all are well-fit with an antipodal decomposition. For the three reference orientations used here, the gravitational wave signal in that direction closely resembles the gravitational wave signal for only a small neighborhood surrounding that point. Results for simulations are estimated using $\simeq 10^4$ candidate viewing directions, each of which includes all $l \leq 4$ contributions to $\psi_4(\hat{n})$.

sion orientations, weighted equally in area; and about 48%, weighted uniformly in ρ^3 (i.e., by equal probability of detection in the local universe). Summing over both antipodal directions, almost all detected emission from a nonprecessing binary is well-fit by either of $\psi_4(\pm\hat{J})$.

By contrast, Figure 4 shows that each of these directions provides a good fit ($P > 0.95$) only for a small area surrounding each reference point. The gravitational wave signal along the (Newtonian) orbital and total angular momentum directions $(\hat{z}, \hat{J})$ are particularly non-representative, reproducing signals emitted only in immediately neighboring directions.

C.   Failure of antipodal reconstruction

Existing gravitational wave searches for nonprecessing binaries, however, do not merely fit each data set against two candidate signals per simulation. Motivated by the simple functional form of mass-quadrupole-dominated emission, real searches *project the data onto the two-dimensional subspace spanned by those two candidates.*[4]

---

[4] Their real and imaginary parts are known as the "cosine" and "sine" chirps. For sufficiently low mass, these two modes are

When the candidate signals are associated with two different antipodal emission directions ($\pm\hat{v}$) we will denote this procedure an *antipodal decomposition.*

Algebraically, an antipodal decomposition estimates the Weyl scalar along any direction via a projection to the subspace spanned by the two antipodes:

$$|N\rangle \equiv \psi_4(\hat{v})/|\psi_4(\hat{v})| \tag{14}$$

$$|S\rangle \equiv \psi_4(-\hat{v})/|\psi_4(-\hat{v})| \tag{15}$$

$$\begin{bmatrix} \rho_N \\ \rho_S \end{bmatrix} = \begin{bmatrix} (N, \psi_4(\hat{n})) \\ (S, \psi_4(\hat{n})) \end{bmatrix} \tag{16}$$

$$\psi_{4est} \equiv \mathcal{P}\psi_4$$
$$\frac{[(\rho_N - (S, N)\rho_S)|N\rangle + (\rho_S - (N, S)\rho_N)|S\rangle]}{1 - |(N, S)|^2} \tag{17}$$

$$\rho_{rem}^2 \equiv |\psi_4 - \psi_{4est}|^2 = (\psi_4, (1 - \mathcal{P})\psi_4)$$
$$= \rho^2 - \frac{|\rho_N|^2 + |\rho_S|^2 - 2\text{Re}(N, S)\rho_N\rho_S^*}{1 - |(N, S)|^2} \tag{18}$$

Practically, an antipodal projection of this kind is useful if the relative loss of SNR is small (i.e., $\rho_{rem}/\rho < 0.05$).

For nonprecessing signals, the success of an antipodal approximation along nearly *any* axis is guaranteed by parameter counting. Comparable-mass nonprecessing binaries are dominated by just two modes (the $(l, m) = (2, 2)$ and $(2, -2)$ modes), with two coefficient functions $\psi_{42\pm2}$. As any antipodal basis are in their span, an antipodal decomposition just corresponds to a change of basis. For nonprecessing binaries, however, the choice $\hat{v} = \hat{J}$ produces added benefits: the antipodes are local extrema of $|\psi_4|$, $dE/dtd\Omega$, and ρ^2. In this frame, trivially the angular dependence of $\rho_{N,S}(\hat{n})$ decomposes into roughly two spin-weighted harmonics, to the extent that higher harmonics can be neglected. Finally, as noted previously this antipodal decomposition is *physical*: the ratio ρ_N/ρ_S is in one-to-one relation with the inclination.

By constrast, for precessing binaries the signal space generally has at least $5(= 2\times2+1)$ basis vectors and thus has 5 complex (10 real) dimensions [47]. The precession of *instantaneous* $(2, 2)$ and $(2, -2)$ modes aligned with L projects into other $l = 2$ modes in the global frame. As a result, the "remaining signal power" ρ_{rem} left after an antipodal decomposition is generally nonzero and often significant, if either precession occurs or if higher harmonics contribute significantly to overall radiation.

Nonprecessing binaries also emit a significant fraction of their total (band-limited) signal ρ^2 in higher harmonics, at high mass [40] or mass ratio [5, 46]. However, comparable-mass nonprecessing binaries are often still well-approximated as antipodal: for most masses, they emit most strongly in two complex-conjugate $l = |m|$

---

nearly orthogonal. Their orthogonality can be exploited to efficiently maximize in time and "coalescence phase" [12]. At high mass too few cycles exist to guarantee orthogonality of the $(2, 2)$ and $(2, -2)$ modes in general.

l	m	$(\rho_{lm}/\bar\rho)^2$ precessing	$(\rho_{lm}/\bar\rho)^2$ nonprecessing
2	2	0.43	0.44
2	-2	0.39	0.44
2	1	0.067	0.01
2	-1	0.010	0.01
2	0	0.009	10^{-4}
3	3	0.039	0.045
3	-3	0.037	0.045
4	4	0.005	0.007
4	-4	0.005	0.007

TABLE I: **Multiple harmonics contribute significantly** to the orientation-averaged signal power, for our reference simulation and mass ($100 M_\odot$). This table refers to mode amplitudes in a frame aligned with the prinicipal axis of $\langle L_{(a} L_{b)} \rangle_M$. The second and third columns show results for our two fiducial simulations, both with $q = 4$ but one precessing and one without any spin. At this mass ratio, both nonprecessing and precessing binaries have observationally significant power in higher modes; see, e.g., Table V in Hannam et al. [5].

modes, with $|m| < l$ suppressed. By contrast, precession ensures that all five $l = 2$ modes are strongly excited, for all masses.

For this simulation and reference mass ($100 M_\odot$) in particular, antipodal decompositions always lose SNR for a significant fraction of orientations. One way to see this is by example, decomposing the waveform along $\hat{z}, \hat{J}, \hat{V}$ in an antipodal decomposition, using each of the other combinations as a basis. None of these directions provides an adequate antipodal basis for reconstructing the waveform along the others. More abstractly, antipodal decompositions fail when, even adopting a well-chosen frame (primed, below) to define the mode basis, a significant fraction of the orientation-averaged signal power [40]

$$\bar\rho^2 \equiv \int (\psi_4, \psi_4) \frac{d\Omega}{4\pi}$$
$$= \sum_{lm} \frac{1}{4\pi} (\psi_{4lm}, \psi_{4lm}) \equiv \sum_{lm} \rho_{lm}^2 \qquad (19)$$

comes from harmonics other than the $(2,2)'$ and $(2,-2)'$ modes. For this simulation and reference mass, the orientation-averaged SNR $\bar\rho$ for a source at $100\,\mathrm{Mpc}$ is $\simeq 25$. Using a (primed) frame aligned with $\hat{V}$, at least nine modes contribute significantly ($> 0.5\%$, summing to $\simeq 99\%$) to $\bar\rho^2$; see Table I. In other words, for this simulation and reference mass, other harmonics invariably contribute a significant fraction of the signal power, for many significant lines of sight.

We have chosen a relatively low reference mass ($100 M_\odot$), for which higher-order multiples $l > 2$ produce a relatively small fraction of the orientation-averaged SNR ($\bar\rho$). At higher masses, higher-order multipoles will produce even larger fractions of the total power [40] and

can lead to greater breakdowns of antipodal approximations.

To summarize, many simplifications extensively employed for nonprecessing binaries break down completely for generic mergers. In general one cannot usefully approximate the line-of-sight gravitational waveform with just two basis functions. As illustrated Table I for this concrete example, the $|m| = 2$ subspace is often but generally need not be the most significant feature. For a nonprecessing binary dominated by the $(2,2)$ and $(2,-2)$ modes, the real and imaginary parts of the waveform along the z axis are proportional to the real and imaginary parts of $e^{2i\Phi_o}$ and therefore are related by a simple phase shift: the signal ($\psi_4(\hat{z}, \Phi_o)$) produced by a binary with initial orbital phase Φ_o is a phase shift by $\pi/4$ ($-i\psi_4(\hat{z}, \Phi_o + \pi/4)$) of the signal produced by a binary starting with a similarly shifted binary phase. By contrast, for a generic binary, multiple harmonics contribute significantly; for nearly no line of sight does the simple phase-shift relationship described above hold to the accuracy needed for gravitational wave data analysis. One cannot maximize over the orbital reference phase Φ_o using an antipodal projection to extract coefficients of the "cosine and sine chirps". The relevant maximum over coaelscence phase can be found only if all harmonics are included [46].

D. Constrained projections onto all harmonics

More broadly, the signal from precessing binaries can be projected onto a higher-dimensional basis. As only four degrees of freedom are needed to specify the line of sight (two euler angles, polarization, and distance to the source), the use of $N > 4/2$ basis vectors requires $N - 2$ complex ($2(N-2)$ real) constraints, to insure the reconstructed signal estimate is consistent with what could generate it.

Broadly speaking, constrained maximization methods have been extensively explored in gravitational wave data analysis. Constrained maximization methods are primarily employed in the context of interpolating a signal manifold using a basis [48, 49]. One particularly relevant example is Pan et al. [47], who describe a strategy for detecting generic precessing low-mass binaries that, for each binary, finds the best-possible line of sight from the binary by first projecting data onto 5 basis signals, then solving constraint equations. In a similar fashion, the single orientation of a particular simulation that best fits a candidate signal can be recovered by projecting onto a simulation's harmonics. As our example illustrates above, at least five and often more basis functions are required per simulation, with the number increasing rapidly with mass as higher harmonics become more significant in band [40]. However, in principle no obstacle exists to constrained maximization over source orientation in an arbitrary reference frame.

In practice, we expect that constrained maximiza-

tion of source orientation should be simplest in a frame aligned with the contours of source signal to noise (ρ^2) and therefore in a frame roughly aligned with $\hat{V}$, the principal eigendirection of $\left\langle L_{(a}L_{b)}\right\rangle_M$.[5] In this frame, the hermetian overlap matrix C_{AB} should generally have the simplest possible form

$$C_{AB}^{-1} \equiv (A, B) \tag{20}$$

where A is shorthand for normalized basis functions of time, proportional to a subset of $\psi_{4lm}(t)$. As a concrete example, the eigenvectors of C_{AB} using the $l = 2$ basis states and our fiducial binary are fairly close to the basis states themselves. The reconstruction process for $\psi_4(\hat{n})$ involves C explicitly and C^{-1} implicitly:

$$\psi_4(\hat{n}) = C_{AB}\rho_B(\hat{n})|B\rangle \tag{21}$$
$$\rho_A \equiv (A, \psi_4) \tag{22}$$

The four free parameters in the signal enter through expressions involving C^{-1}. First, the parameters ρ_A must reproduce the total signal $\rho^2 \equiv (\psi_4, \psi_4)$ along this line of sight, or

$$\rho^2 = \rho_A^* C_{AB}^{-1} \rho_B \tag{23}$$

The remaining three parameters correspond to specifying the orientation of the source, with three Euler angles. Two of the Euler angles can be specified using the principal axes of $\left\langle L_{(a}L_{b)}\right\rangle_M$, which has the form

$$\left\langle L_{(a}L_{b)}\right\rangle_M = \frac{C_{AB}^{-1}}{\rho^2}\left[\int d\Omega(\rho_A(\hat{n})^* \mathcal{L}_a \mathcal{L}_b \rho_B(\hat{n}))\right] \tag{24}$$

The remaining Euler angle, the polarization angle, is connected to the phase of ρ. Though we adopt a multipolar basis in *angle* to define the basis set in *time*, the time domain basis functions $|A\rangle$ are not generally orthogonal, so $\rho_A(\hat{n})$ are generally not proportional to spin-weighted harmonics.[6] Conversely, only parameters in the corresponding 4-dimensional submanifold of the $2N$ (real) dimensional space are consistent reconstructions of ψ_4 from this source.

Therefore, the overlap matrix C of the time-domain basis coefficients enters naturally into all reconstructions and constraints. Their underlying algebra will be simplest if this $N \times N$ complex matrix takes block diagonal form. However, our arguments above suggest that no fixed reference frame, not even one aligned with J, will make C block diagonal at all masses.

---

[5] For the purposes of this paper, we discuss constrained maximization of source orientation, assuming all harmonics are known from simulations or post-Newtonian calculations. More broadly, by suitable interpolation across all masses and spins, a similar process of constrained maximization may allow waveform catalogs to reconstruct all the basis waveforms of precessing binaries.

[6] In special cases such as nonprecesing inspiralling binaries, the time-domain basis functions are orthogonal and ρ_A are proportional to spin-weighted harmonics. In this special case, the integral on the right can be evaluated using representation theory of SU(2) [21].

IV. CONCLUSIONS

Merging black hole binaries produce complicated orientation-dependent emission. For nonprecessing binaries, the orbital angular momentum defines a preferred orientation. For these simple binaries, a generic signal can be well-approximated by a linear combination of $\psi_4(\hat{L})$ and $\psi_4(-\hat{L})$, or just one of the two functions $\psi_4(\pm\hat{L})$ away from the orbital plane. We demonstrate that these simplifying approximations break down for generic precessing binaries, by comparing different short, high-mass merger signals extracted along different orientations, using an extremely loose, data-analysis-motivated discriminator. Notably, our example shows that the final black hole spin angular momentum axis is emphatically *not* the natural emission orientation at late times.

For nonprecessing and some precessing binaries, most detection-weighted gravitational wave signal power (ρ^2) is radiated along the total angular momentum axis. Our counterexample also demonstrates that neither J, L, nor S generally corresponds to the direction of largest detectable gravitational wave signal. By contrast, the peak of SNR (ρ^2) versus orientation is nearly along the dominant eigendirection of $\left\langle L_{(a}L_{b)}\right\rangle_M$ [21].

For nonprecessing binaries, the orbit and kinematics define a preferred symmetry axis, relative to which the modulations encoded in the waveform appear particularly simple. For generic precessing binaries, particularly during the merger phase, different physical concerns (kicks; precession) lead to different preferred orientations.

For data analysis purposes, we recommend an orientation along the peak of the network-weighted SNR along the line of sight (ρ^2) or the nearly-identical location identified by the principal eigenvalue of $\left\langle L_{(a}L_{b)}\right\rangle_M$. This frame will change with mass. However, we anticipate PTF-style constrained maximizations over source orientations will generally be simpler in this frame. We will discuss the differences between this choice and the standard frame in a subsequent publication.

The breakdown of J as a preferred orientation comes as no surprise. As an extreme example, for sufficiently extreme-mass ratio binaries, the total angular momentum is always dominated by the black hole spin, carrying no information whatsoever about the motion. In fact, the relevant preferred orientation depends on how the detector "averages" the orbit. As a less extreme example, for BH-NS binaries, the orbital angular momentum direction is the preferred direction on any sufficiently short timescale. For binaries whose masses and spins allow significant evolution in band, the relevant orientation will become (roughly) a time-average of that vector [21]. Only if the orbital angular momentum precesses frequently about the total angular momentum *in band* will the total angular momentum arise as a preferred orientation. Even for high-mass-ratio binaries, precession can be irrelevant if it occurs out of band (e.g., before the

detected merger signal).

Finally, in this paper we introduced several concepts useful for interpreting the signal from precessing, unequal-mass binaries. First and foremost, we describe a complex overlap and its natural maximization in time and *polarization*, a tool which efficiently eliminates two extrinsic parameters of generic signals even in the presence of higher harmonics. Second, we emphasize that ψ_4, being spin-weighted, naturally divides into two chiral parts; this decomposition corresponds to positive and negative frequency in the fourier domain.

Appendix A: Chiral-weighted Orientation

In general, the two extrema of ρ^2 need not be antipodal. Some methods for determining "the" optimal emission direction treat $\hat{n}$ and $-\hat{n}$ symmetrically. To allow for different orientations of these two poles, we generalize the tensor $\langle L_{(a}L_{b)}\rangle_M$ introduced previously to treat contributions from $+$ and $-$ helicities separately, if desired. For example, a matrix that sums up contributions from only right-handed emission is

$$\langle L_{(a}L_{b)}\rangle_{M,+} = \frac{\int_0^\infty df \int d\Omega \tilde{\psi}_4^*(f) L_{(a}L_{b)}\tilde{\psi}_4(f)/S_h}{\int_0^\infty df \int d\Omega |\tilde{\psi}_4(f)|^2/S_h} \quad \text{(A1)}$$

This construct correctly identifies the asymmetric extrema of $\rho_\pm$ seen in even nonprecessing binaries; see, e.g., the red dot in the bottom panel of Figure 2.

Appendix B: Complex overlap and antipodal decomposition for symmetric quadrupole-dominated emission

When one or a handful of modes dominates, the angular dependence of the overlap $P(\hat{n}, \hat{n}')$ can be approximated everywhere via a handful of global coefficients. As a practical example, if ψ_4 is dominated by symmetric $l = |m| = 2$ emission in the reference frame, the Weyl scalar can be expanded ψ_4 as

$$\psi_4 = \psi_{422}(t)Y_{22}^{(-2)}(\hat{n}) + \psi_{422}(t)^* Y_{2-2}^{(-2)}(\hat{n}) \quad \text{(B1a)}$$

$$P_{22} \equiv (\psi_{422}, \psi_{422})/|\psi_{422}|^2 = 1 \quad \text{(B1b)}$$

where we have required the two antipodal terms to be complex conjugates, as for a nonprecessing signal. In terms of these coefficients, we find the overlap $P(\hat{n}, \hat{n}')$ (before maximizing over time and phase) can be well approximated by

$$\begin{aligned} P &\simeq |P_{22}|\frac{\left[Y_2^* Y_2' + Y_{-2}^* Y_{-2}'\right]}{\sqrt{(|Y_2|^2 + |Y_{-2}|^2)(|Y_2'|^2 + |Y_{-2}'|^2)}} \\ &+ O((\psi_{422}, \psi_{4_{22}}^*)) \quad \text{(B1c)} \\ &= \frac{e^{2i\phi}Y_2(\theta)Y_2(\theta') + e^{-2i\phi}Y_{-2}(\theta)Y_{-2}(\theta')}{\sqrt{(|Y_2(\theta)|^2 + |Y_{-2}(\theta)|^2)(|Y_2(\theta')|^2 + |Y_{-2}(\theta')|^2)}} \end{aligned}$$

where we use the shorthand $Y_m \equiv Y_{2m}^{(-2)}(\hat{n})$ and similarly for Y_m' to reduce superfluous subscripts and where in the last line we factor out the common $e^{im\phi}$ from $Y_{lm}^{(-2)}$. In the above expression we assume rapidly oscillating, opposite-chirality terms like $(\psi_{422}, \psi_{4_{22}}^*)$ cancel.[7] We also make the trivial observation that the normalized overlap of a signal with itself is unity ($P_{22} = 1$). This purely geometrical expression is largest when the two vectors are coaligned with their respective reference frames (i.e., when $\theta = \theta' = 0$). As an example, the special case of $\theta' = 0$ has the form

$$|P(\hat{z}, \hat{n})| = \frac{\cos^4 \theta/2}{\sqrt{\cos^8 \theta/2 + \sin^8 \theta/2}} \quad \text{(B2)}$$

[1] J. Centrella, J. G. Baker, B. J. Kelly, and J. R. van Meter, Reviews of Modern Physics **82**, 3069 (2010), 1010.5260.

[2] J. G. Baker, J. R. van Meter, S. T. McWilliams, J. Centrella, and B. J. Kelly, Physical Review Letters **99**, 181101 (2007), arXiv:gr-qc/0612024, URL http://xxx.lanl.gov/abs/gr-qc/0612024.

[3] M. Boyle, D. A. Brown, L. E. Kidder, A. H. Mroué, H. P. Pfeiffer, M. A. Scheel, G. B. Cook, and S. A. Teukolsky, Phys. Rev. D **76**, 124038 (2007), arXiv:0710.0158.

[4] M. Hannam, S. Husa, J. A. González, U. Sperhake, and B. Brügmann, Phys. Rev. D **77**, 044020 (2008), 0706.1305, URL http://xxx.lanl.gov/abs/arXiv:0706.1305.

[5] M. Hannam, S. Husa, F. Ohme, D. Müller, and B. Brügmann, Phys. Rev. D **82**, 124008 (2010), 1007.4789, URL http://xxx.lanl.gov/abs/arXiv:1007.4789.

[6] A. Buonanno, Y. Pan, J. G. Baker, J. Centrella, B. J. Kelly, S. T. McWilliams, and J. R. van Meter, Phys. Rev. D **76**, 104049 (2007), 0706.3732, URL http://xxx.lanl.gov/abs/arXiv:0706.3732.

[7] I. MacDonald, S. Nissanke, and H. P. Pfeiffer, Classical and Quantum Gravity **28**, 134002 (2011), 1102.5128.

[8] F. Ohme, M. Hannam, and S. Husa, Phys. Rev. D **84**, 064029 (2011), 1107.0996, URL http://xxx.lanl.gov/abs/arXiv:1107.0996.

[9] L. Santamaria, F. Ohme, P. Ajith, B. Bruegmann, N. Dorband, M. Hannam, S. Husa, P. Moesta, D. Pollney, C. Reisswig, et al., (arXiv:1005.3306) (2010), URL http://xxx.lanl.gov/abs/arXiv:1005.3306.

[10] P. Ajith, M. Hannam, S. Husa, Y. Chen, B. Brügmann, N. Dorband, D. Müller, F. Ohme, D. Pollney, C. Reisswig, et al., Physical Review Letters **106**, 241101 (2011), 0909.2867, URL http://xxx.lanl.gov/abs/arXiv:0909.2867.

[11] R. Sturani, S. Fischetti, L. Cadonati, G. M. Guidi, J. Healy, D. Shoemaker, and A. Viceré, Journal of Physics Conference Series **243**, 012007 (2010), 1005.0551.

[12] B. A. Allen, W. G. Anderson, P. R. Brady, D. A. Brown, and J. D. E. Creighton (2005), gr-qc/0509116.

[13] D. Brown, A. Lundgren, and R. O'Shaughnessy, in preparation (????).

[14] T. A. Apostolatos, C. Cutler, G. J. Sussman, and K. S. Thorne, Phys. Rev. D **49**, 6274 (1994).

[15] L. Rezzolla, Classical and Quantum Gravity **26**, 094023 (2009), 0812.2325.

[16] C. O. Lousto, M. Campanelli, Y. Zlochower, and H. Nakano, Classical and Quantum Gravity **27**, 114006 (2010), 0904.3541.

[17] L. Boyle and M. Kesden, Phys. Rev. D **78**, 024017 (2008), 0712.2819.

[18] P. Schmidt, M. Hannam, S. Husa, and P. Ajith, Phys. Rev. D **84**, 024046 (2011), 1012.2879, URL http://xxx.lanl.gov/abs/arXiv:1012.2879.

[19] M. Boyle, R. Owen, and H. P. Pfeiffer, Phys. Rev. D **84**, 124011 (2011), 1110.2965.

[20] C. M. Will and A. G. Wiseman, Phys. Rev. D **54**, 4813 (1996).

[21] R. O'Shaughnessy, B. Vaishnav, J. Healy, Z. Meeks, and D. Shoemaker, Phys. Rev. D **84**, 124002 (2011), 1109.5224, URL http://link.aps.org/doi/10.1103/PhysRevD.84.124002.

[22] M. van der Sluys, V. Raymond, I. Mandel, C. Röver, N. Christensen, V. Kalogera, R. Meyer, and A. Vecchio, Classical and Quantum Gravity **25**, 184011 (2008), 0805.1689.

[23] V. Raymond, M. V. van der Sluys, I. Mandel, V. Kalogera, C. Röver, and N. Christensen, Classical and Quantum Gravity **26**, 114007 (2009), 0812.4302.

[24] C. Röver, R. Meyer, and N. Christensen, Phys. Rev. D **75**, 062004 (2007), arXiv:gr-qc/0609131.

[25] R. N. Lang, S. A. Hughes, and N. J. Cornish, Phys. Rev. D **84**, 022002 (2011), 1101.3591.

[26] B. Aylott, B. Farr, V. Kalogera, I. Mandel, V. Raymond, C. Rodriguez, M. van der Sluys, A. Vecchio, and J. Veitch, ArXiv e-prints (2011), 1106.2547.

[27] S. Nissanke, J. Sievers, N. Dalal, and D. Holz, Astrophys. J. **739**, 99 (2011), 1105.3184.

[28] F. Herrmann, I. Hinder, D. Shoemaker, and P. Laguna, Classical and Quantum Gravity **24**, S33 (2007), arXiv:gr-qc/0601026.

[29] F. Herrmann, I. Hinder, D. M. Shoemaker, P. Laguna, and R. A. Matzner, Phys. Rev. **D76**, 084032 (2007), 0706.2541.

[30] F. Herrmann, I. Hinder, D. Shoemaker, P. Laguna, and R. A. Matzner, Astrophys. J. **661**, 430 (2007), gr-qc/0701143.

[31] I. Hinder, B. Vaishnav, F. Herrmann, D. Shoemaker, and P. Laguna, Phys. Rev. **D77**, 081502 (2008), 0710.5167.

[32] J. Healy et al., Phys. Rev. Lett. **102**, 041101 (2009), 0807.3292.

[33] I. Hinder, F. Herrmann, P. Laguna, and D. Shoemaker, **arxiv:0806.1037** (2008), 0806.1037.

[34] J. Healy, J. Levin, and D. Shoemaker, Phys. Rev. Lett. **103**, 131101 (2009), 0907.0671.

[35] J. Healy, P. Laguna, R. A. Matzner, and D. M. Shoemaker, Phys. Rev. **D81**, 081501 (2010), 0905.3914.

[36] T. Bode, R. Haas, T. Bogdanovic, P. Laguna, and D. Shoemaker, Astrophys. J. **715**, 1117 (2010), 0912.0087.

[37] E. Schnetter, S. H. Hawley, and I. Hawke, Class. Quant. Grav. **21**, 1465 (2004).

[38] cactus-web, cactus Computational Toolkit home page: http://www.cactuscode.org.

[39] S. Husa, I. Hinder, and C. Lechner, Computer Physics Communications **174**, 983 (2006).

[40] R. O'Shaughnessy, B. Vaishnav, J. Healy, and D. Shoemaker, Phys. Rev. D **82**, 104006 (2010), (arXiv:1007.4213), URL http://xxx.lanl.gov/abs/arXiv:1007.4213.

[41] P. Ajith and S. Bose, Phys. Rev. D **79**, 084032 (2009), 0901.4936.

[42] B. Vaishnav, I. Hinder, F. Herrmann, and D. Shoemaker, Phys. Rev. D **76**, 084020 (2007), 0705.3829.

[43] C. Cutler and E. E. Flanagan, Phys. Rev. D **49**, 2658 (1994), gr-qc/9402014.

[44] "Gravitational wave international committee" (2010), URL https://gwic.ligo.org/roadmap/.

[45] B. F. Schutz, Classical and Quantum Gravity **28**, 125023 (2011), 1102.5421.

[46] S. T. McWilliams, B. J. Kelly, and J. G. Baker, Phys. Rev. D **82**, 024014 (2010), 1004.0961, URL http://xxx.lanl.gov/abs/arXiv:1004.0961.

[47] Y. Pan, A. Buonanno, Y. Chen, and M. Vallisneri, Phys. Rev. D **69**, 104017 (2004), URL http://xxx.lanl.gov/abs/gr-qc/0310034.

[48] K. Cannon, A. Chapman, C. Hanna, D. Keppel, A. C. Searle, and A. J. Weinstein, Phys. Rev. D **82**, 044025 (2010), 1005.0012.

[49] S. E. Field, C. R. Galley, F. Herrmann, J. S. Hesthaven, E. Ochsner, and M. Tiglio, (arXiv:1101.3765) (2011), URL http://xxx.lanl.gov/abs/arXiv:1101.3765.

Erratum : Is J enough? Comparison of gravitational waves emitted along the total angular momentum direction with other preferred orientations

R. O'Shaughnessy

Center for Gravitation and Cosmology, University of Wisconsin-Milwaukee, Milwaukee, WI 53211, USA[*]

J. Healy, L. London, Z. Meeks, and D. Shoemaker

Center for Relativistic Astrophysics, Georgia Tech, Atlanta, GA 30332, USA

The algorithm used to reconstruct $\psi_{4,lm}$ to $\psi_4(\theta, \phi)$ in post-processing used a different convention for the spin-weighted spherical harmonics than the convention used to do the decomposition. Physically, this difference corresponds to rotating the simulation results by 180° about the $\hat{z}$ axis. In this paper we performed all calculations starting with that codes' multipolar output. As a result, all tensors and preferred directions derived from the original code were rotated by 180° relative to the simulation's frame. By contrast, the total initial and final angular momentum was correctly calculated, leading to a discrepancy between the relative orientation of our preferred direction and the quantity we compared to. Figures 1, 2, and 4 must be replaced, as the relative orientation of $\hat{J}, \hat{L}$ (simulation frame) versus the contours of ψ and $\hat{V}$ (waveform frame) change. Figure 3, as a qualitative illustration of the differences between the real and complex overlap, undergoes a trivial relabelling of the ϕ axis. Table 1 remains unchanged.

Figures 1 and 2 now show $\hat{J}$ is much closer to two key features extracted from outgoing radiation: first, our preferred direction (blue line), which now precesses around J; and second, the largest values of $|\psi_4|$ and $dE/d\Omega$. In Figure 4, the blue line showing the cumulative distribution of $P(\hat{J}, \hat{n})$ now more closely resembles the black line showing the cumulative distribution of $P(V^*, \hat{n})$.

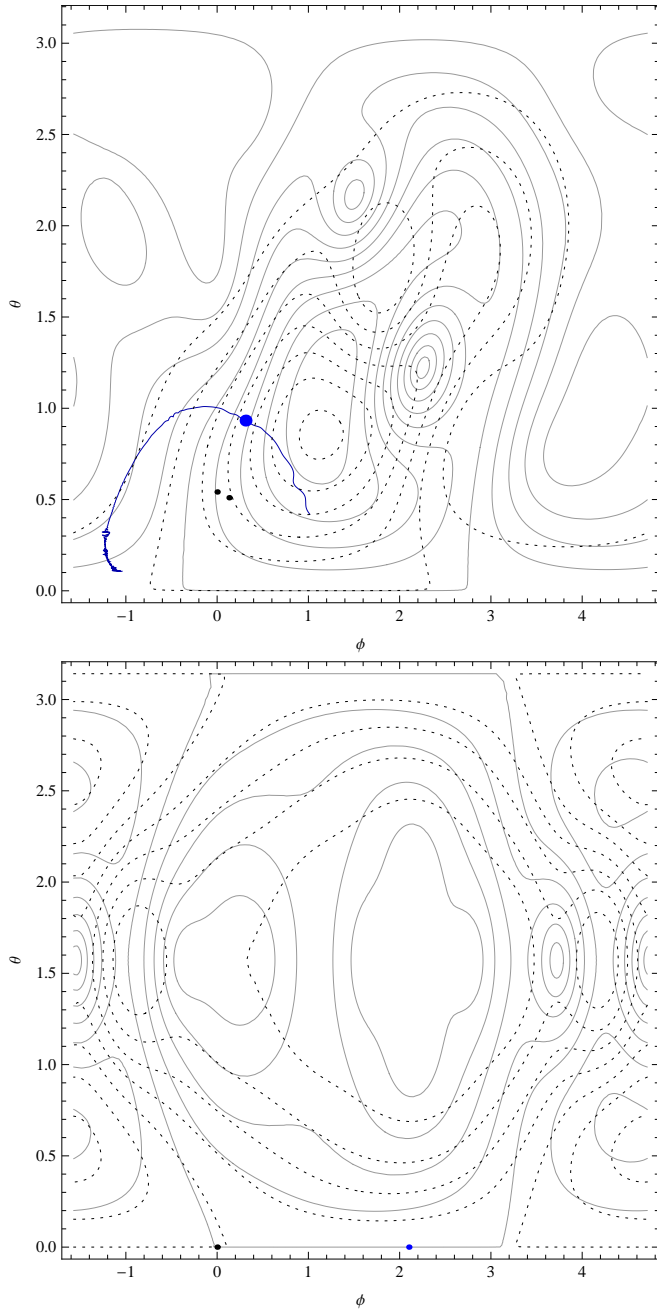The conclusions of the paper remain unchanged.

FIG. 1: **Time-domain contours** of $|\psi_4|$ (solid) and $dE/dtd\Omega$ (dashed), evaluated at the peak of the $(l,m) = (2,2)$ mode. Both quantities are normalized to 1 at $\theta = \phi = 0$. Solid black dots indicate the location of the initial and final total angular momenta. The solid blue dot indicates the preferred axis identified by $\left\langle L_{(a}L_{b)}\right\rangle_t$ at this time. The dark blue path indicates how this preferred orientation evolves with time, several hundred M before and $30M$ after this reference time. The *top panel* corresponds to the fiducial spinning binary. The bottom panel shows a binary with comparable mass ratio $(m_1/m_2 = 4)$ but without any spin.
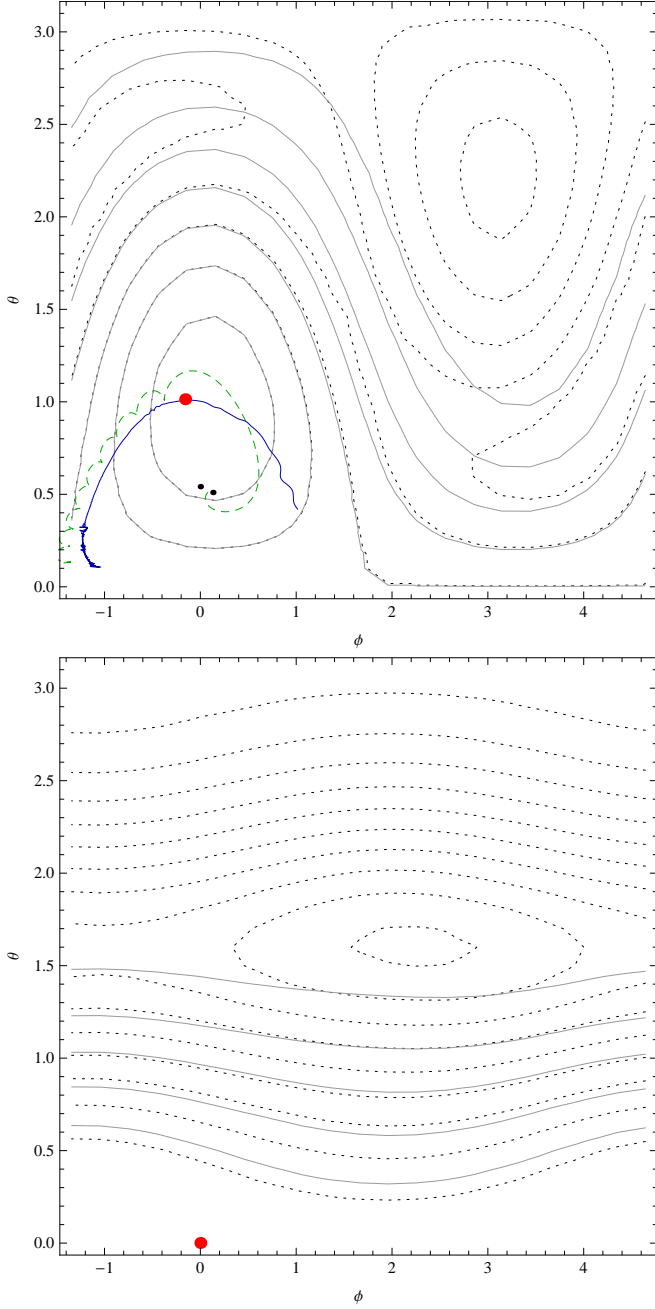
FIG. 2: **Detector-weighted contours** of ρ (dotted) and ρ_+ (solid), evaluated at $M = 100M_\odot$, plotted versus the simulation's asymptotic spherical polar coordinates (i.e., aligned with the initial orbital angular momentum). Solid black dots indicate the location of the initial and final total angular momenta. The solid red dot indicates the preferred axis identified by $\left\langle L_{(a}L_{b)} \right\rangle_{M,+}$ [Eq. (**??**)] at this time; nearly identical preferred axes are identifies by $\left\langle L_{(a}L_{b)} \right\rangle_M$ and $\left\langle L_{(a}L_{b)} \right\rangle_{M-}$. As in Fig. 1, the solid blue path indicates the evolution of $\left\langle L_{(a}L_{b)} \right\rangle$ versus time. The dashed green path indicates the orientation of the (Newtonian, coordinate) orbital angular momentum $\propto \mathbf{r} \times \mathbf{v}$. The *top panel* corresponds to the fiducial spinning binary, while the *bottom panel* shows an nonspinning binary with comparable mass ratio ($q = 4$). In the bottom panel, the preferred orientation identified by $\left\langle L_{(a}L_{b)} \right\rangle_{M,+}$ is slightly above the $\theta = 0$ line; the two directions identified by $\left\langle L_{(a}L_{b)} \right\rangle_{M,\pm}$ are not precisely antipodal.
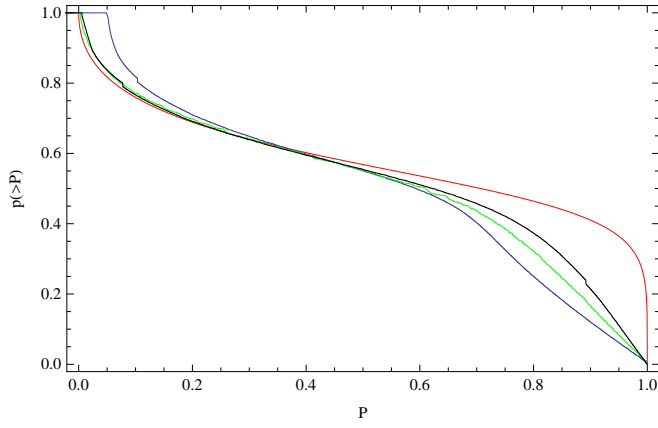
FIG. 3: **Area of high overlap**: Fraction p of the sphere for which the overlap $P_{max}(\hat{v}, \hat{n})$ is above a given threshold P, versus the threshold, for $\hat{v} = \hat{z}$ (blue), $\hat{J}$ (green), and the preferred axis of $\left\langle L_{(a} L_{b)} \right\rangle_M$ (black). For comparison, the thin red curve shows the corresponding result for a binary radiating only conjugate and orthogonal $(2, 2)$ and $(2, -2)$ modes and a reference axis $\hat{v} = \hat{z}$; see the appendix for a derivation. For this idealized nonprecessing binary, more than a third of all orientations have better than $P = 0.95$ (complex) match with the $(2, 2)$ mode; all are well-fit with an antipodal decomposition. For the three reference orientations used here, the gravitational wave signal in that direction closely resembles the gravitational wave signal for only a small neighborhood surrounding that point. Results for simulations are estimated using $\simeq 10^4$ candidate viewing directions, each of which includes all $l \leq 4$ contributions to $\psi_4(\hat{n})$.